

# Fusing Nanowires into Thin Films: Fabrication of Graded-Heterojunction Perovskite Solar Cells with Enhanced Performance

Yi Zhang, Hanjun Yang, Min Chen, Nitin P. Padture,\* Ou Chen,\* and Yuanyuan Zhou\*

Perovskite solar cells (PSCs) have recently experienced a rapid rise in power conversion efficiency (PCE), but the prevailing PSCs with conventional mesoscopic or planar device architectures still contain nonideal perovskite/hole-transporting-layer (HTL) interfaces, limiting further enhancement in PCE and device stability. In this work, CsPbBr<sub>3</sub> perovskite nanowires are employed for modifying the surface electronic states of bulk perovskite thin films, forming compositionally-graded heterojunction at the perovskite/HTL interface of PSCs. The nanowire morphology is found to be key to achieving lateral homogeneity in the perovskite film surface states resulting in a near-ideal graded heterojunction. The hidden role of such lateral homogeneity on the performance of graded-heterojunction PSCs is revealed for the first time. The resulting PSCs show high PCE up to 21.4%, as well as high operational stability, which is superior to control PSCs fabricated without CsPbBr<sub>3</sub>-nanocrystals modification and with CsPbBr<sub>3</sub>-nanocubes modification. This study demonstrates the promise of controlled hybridization of perovskite nanowires and bulk thin films for more efficient and stable PSCs.

state-of-the-art PSCs can be broadly divided into two types, viz., mesoscopic TiO<sub>2</sub>-based PSCs and planar PSCs with only the compact TiO<sub>2</sub> electron-transporting layer (ETL).<sup>[11–14]</sup> However, both types of devices invariably contain a planar heterojunction formed at the interface between the perovskite and the hole-transporting layer (HTL) in PSCs. The energy level of the highest occupied molecular orbital (HOMO) of the commonly used HTL materials such as Spiro-OMeTAD, poly(3-hexylthiophene) and poly(triaryl amine) is about –5.1 eV, which does not match perfectly with the valence band maximum (VBM) of the prototypical methylammonium lead triiodide (CH<sub>3</sub>NH<sub>3</sub>PbI<sub>3</sub> or MAPbI<sub>3</sub>) perovskite, and also many other state-of-the-art halide perovskite compositions.<sup>[15,16]</sup> This limits the open circuit voltage (V<sub>OC</sub>), and, thus, the PCE in these PSCs. Therefore, several studies in the literature have proposed ex

## 1. Introduction

Halide perovskite materials have emerged as a family of semiconductors that are catalyzing a revolution in the field of solar cells, as they offer the promise of low cost and exceptional optoelectronic properties.<sup>[1–4]</sup> The record power conversion efficiency (PCE) of perovskite-based solar cells (PSCs) has climbed rapidly to a certified 23.7%<sup>[5]</sup> since their invention in 2009.<sup>[4]</sup> Such rapid rise of PSCs has been mainly attributed to the significant effort and achievement in controlling the crystallization and microstructures (grains and grain boundaries) of the perovskite thin films.<sup>[6–10]</sup> The commonly used device architectures in the

post facto incorporation of various materials at the perovskite/HTL interfaces to form graded-heterojunction, thereby reducing the energy level mismatch and enhancing the device performance.<sup>[17–20]</sup> However, this strategy always increases the complexity of the devices as well as the processing. In this context, while the most-widely studied halide perovskite is MAPbI<sub>3</sub>, the halide perovskite family has a wide composition space, which allows fine-tuning of electronic structures and properties in the perovskites themselves.<sup>[21–23]</sup> This unique feature of halide perovskite materials provides the opportunity to form graded perovskite–HTL heterojunction simply through compositional engineering of perovskite thin films without the introduction of additional materials.<sup>[24]</sup> However, the fabrication of a perovskite layer with well-controlled graded compositions remains a significant challenge. This is primarily because the use of orthogonal solvents is required for the solution deposition of multilayer perovskite thin films, but all halide perovskites are generally highly soluble in common polar solvents such as dimethylformamide (DMF), dimethyl sulfoxide (DMSO), and *N*-methyl-2-pyrrolidone.<sup>[25]</sup> Previous studies in the literature suggest the feasibility of using perovskite nanocrystals (dispersed in the anti-solvent used during the formation of the perovskite bulk thin films) to tackle this issue.<sup>[20,26–31]</sup> The most representative study is reported by Zai et al.,<sup>[29]</sup> who demonstrated the incorporation of CsPbBr<sub>3</sub> nanocrystals (nanocube morphology) into a bulk MAPbI<sub>3</sub> perovskite thin film, forming a graded heterojunction

Dr. Y. Zhang, M. Chen, Prof. N. P. Padture, Prof. Y. Zhou  
School of Engineering  
Brown University  
Providence, RI 02912, USA  
E-mail: nitin\_padture@brown.edu; yuanyuan\_zhou@brown.edu  
H. Yang, Prof. O. Chen  
Department of Chemistry  
Brown University  
Providence, RI 02912, USA  
E-mail: ouchen@brown.edu

 The ORCID identification number(s) for the author(s) of this article can be found under <https://doi.org/10.1002/aenm.201900243>.

DOI: 10.1002/aenm.201900243

that improved the interfacial band alignment and the PSC PCE. Although this initial effort is very promising, in our study, we have identified a hidden factor—lateral uniformity—in the as-formed graded heterojunction, which has a profound effect on the performance and stability of the final PSC devices. The use of nanocrystals with the conventional nanocube morphology leads only to incomplete passivation and mixed electronic states of the bulk perovskite film surface, thereby limiting the extent of performance enhancement. Strikingly, by replacing nanocrystals with nanowires, this issue is well addressed with the ready and reproducible formation of laterally homogeneous heterojunctions, resulting in significantly improved PSC PCE and operational stability. More importantly, this method is generic, and it can be used for the fabrication of PSCs with various perovskite thin film compositions. For example, the incorporation of CsPbBr<sub>3</sub> nanowires into the mixed-cation halide perovskite (MA<sub>0.3</sub>FA<sub>0.7</sub>PbI<sub>3</sub>) bulk thin films leads to PSCs with PCE as high as 21.4%.

## 2. Results and Discussion

CsPbBr<sub>3</sub> perovskite nanocubes (NCs) and nanowires (NWs) were synthesized using modified methods that have been reported in the literature.<sup>[28,32–34]</sup> CsPbBr<sub>3</sub> is chosen due to its structural similarity with MAPbI<sub>3</sub>, small lattice mismatch (5.9%), high stability, and ease of synthesis. **Figure 1a** and **b** are transmission electron microscope (TEM) images of the as-synthesized CsPbBr<sub>3</sub> NCs and NWs, respectively, showing high uniformity in size and shape. The average edge length of CsPbBr<sub>3</sub> NCs is determined to be 8.5 ± 0.7 nm (**Figure 1a**). The average length of the NWs is 95 ± 42 nm, with an average

diameter of 2.5 ± 0.5 nm (**Figure 1b**). **Figure 1c** shows UV–vis absorption and photoluminescence (PL) spectra of the CsPbBr<sub>3</sub> NCs and NWs. Multiple electronic transition features with sharp PL profiles indicate mono-dispersity in the CsPbBr<sub>3</sub> NCs and NWs, which is consistent with the TEM observations (**Figure 1a,b**). The significant blue-shift of both absorption and PL features of the CsPbBr<sub>3</sub> NWs, as compared to the CsPbBr<sub>3</sub> NCs, is attributed to the stronger quantum confinement along the shorter dimension (2.5 nm) of the CsPbBr<sub>3</sub> NWs, which is consistent with previous observations.<sup>[35,36]</sup> **Figure 1d** presents X-ray diffraction (XRD) patterns of CsPbBr<sub>3</sub> NCs and NWs, both of which show characteristic broad 110 and 200 peaks, confirming the purity of the perovskite phase. The XRD peak broadening in the CsPbBr<sub>3</sub> NCs results in a size estimation of 7.8 nm using the Scherer equation (see **Figure S1**, Supporting Information), which is consistent with the TEM results. Note that the peak-broadening method cannot be applied reliably to CsPbBr<sub>3</sub> NWs due to their high aspect ratios.

The as-synthesized CsPbBr<sub>3</sub> NCs or NWs were dispersed in chlorobenzene, forming colloidal suspension for use in the thin film processing. The processing method is illustrated schematically in **Figure 2**. First, the perovskite precursor solution (in DMSO) is spread on the substrate, and then spin-coated. During the spin-coating process, a drop of CsPbBr<sub>3</sub> NCs or NWs colloidal suspension is dripped. The dripped nanocrystals (NCs or NWs) not only serve as heterogeneous nucleation sites for the crystallization of the perovskite-solvent adduct thin films, but are also anchored near the thin film surface. The second step is thermal annealing, which “fuses” the CsPbBr<sub>3</sub> NCs or NWs into the perovskite thin film via diffusion, inducing a gradation of CsPbBr<sub>3</sub>-rich at the top to CsPbBr<sub>3</sub>-lean toward the bottom of the perovskite film.<sup>[37]</sup> This fabrication method is similar to what

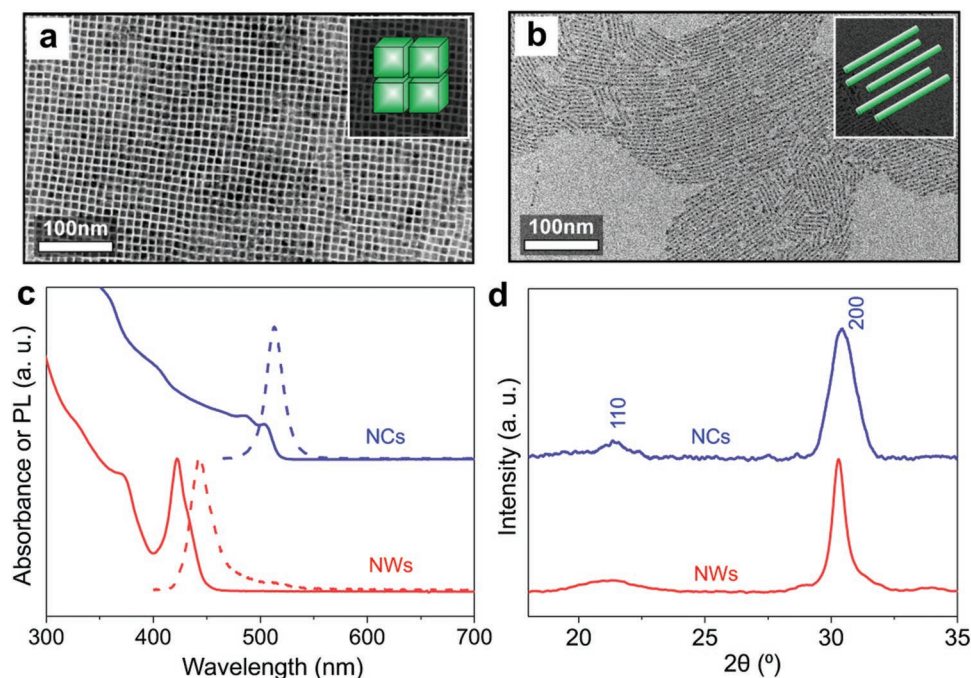


**Figure 1.** Bright-field TEM images of schematic illustrations (insets). a) CsPbBr<sub>3</sub> NCs and b) NWs. c) UV–vis absorption (solid lines) and PL (dashed lines) spectra of CsPbBr<sub>3</sub> NCs and NWs. d) Indexed XRD patterns of CsPbBr<sub>3</sub> NCs and NWs.

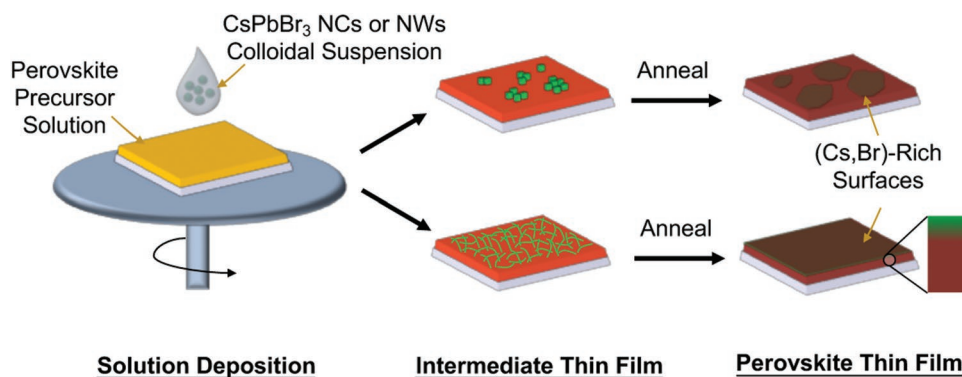


**Figure 2.** Schematic illustration showing the preparation of perovskite thin films with graded incorporation of CsPbBr<sub>3</sub> nanocrystals at the top film surface. The effect of nanocrystal morphology (either nanowire or nanocube) is also illustrated.

was recently reported by Zai et al.<sup>[29]</sup> However, the significant finding here is that the morphology of the CsPbBr<sub>3</sub> nanocrystals plays an important role in determining the distribution of their surface incorporation, which has a profound effect on the properties/performance of the final perovskite thin films and PSCs. Specifically, in the case of NCs incorporation, the NCs tend to aggregate during the dripping step, which correspondingly results in a spatially inhomogeneous distribution on the film surface. In the case of NWs, owing to their superior dispersion (Figure S2, Supporting Information), NWs form uniform interconnected network on the film surface, which then diffuses evenly into the film during annealing to form a uniform layer

with better surface coverage. The size of the NWs may influence this thin film modification process and final device performance, but that study is a topic for future research.

It is worth noting that Chen et al.<sup>[38]</sup> have also used CsPbBr<sub>3</sub> NWs in the context of modifying the MAPbI<sub>3</sub>/HTL interface. However, in that study, the CsPbBr<sub>3</sub> NWs were postdeposited on as-prepared solid MAPbI<sub>3</sub> perovskite thin film, and only physically located on the film surface. Their objective was quite different from that of the present study, where a CsPbBr<sub>3</sub>-NWs assembly was created at the interface to serve as a “grating” for improved light harvesting and efficient fluorescence resonance energy transfer.<sup>[38]</sup>

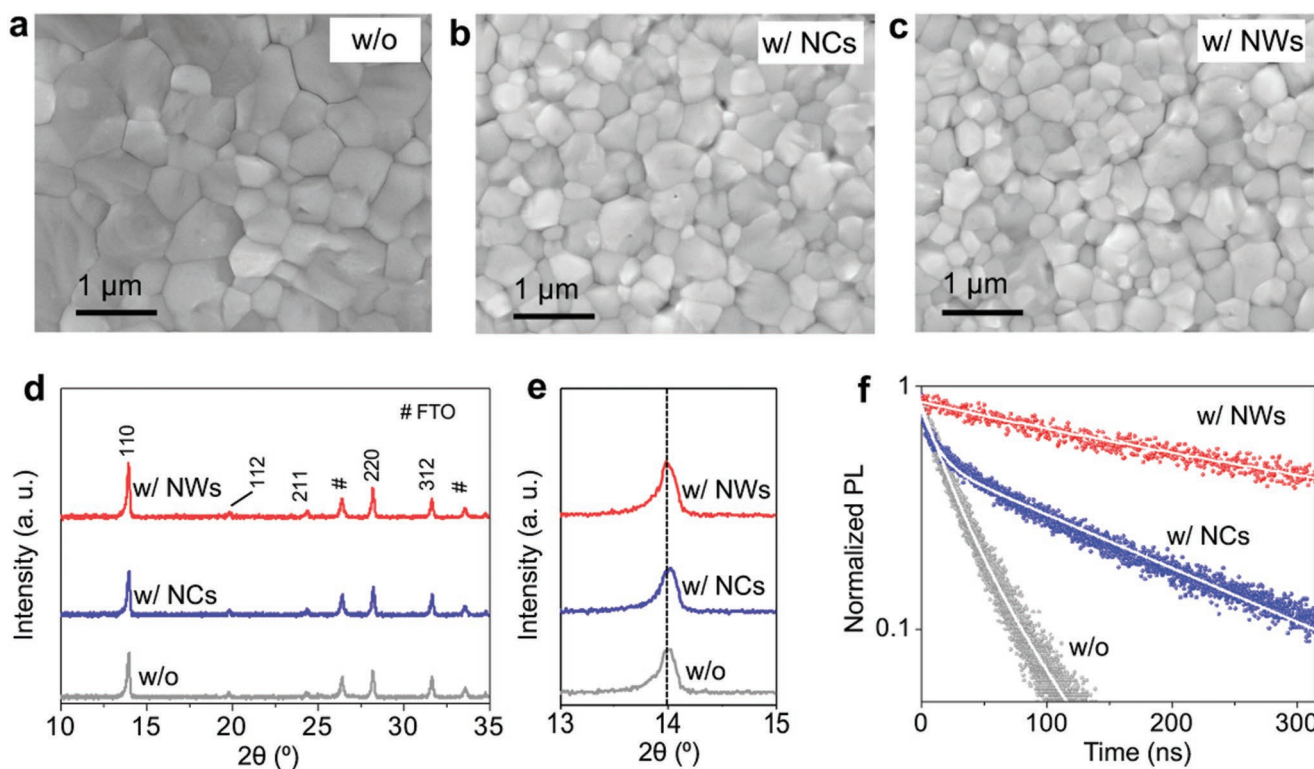


**Figure 3.** Top-view SEM images of the MAPbI<sub>3</sub> perovskite thin films. a) without CsPbBr<sub>3</sub> nanocrystals, b) with CsPbBr<sub>3</sub>-NCs incorporation, and c) with CsPbBr<sub>3</sub>-NWs incorporation. d,e) Indexed XRD patterns and f) time-resolved PL spectra of MAPbI<sub>3</sub> perovskite thin films without and with CsPbBr<sub>3</sub> NCs or NWs incorporation.

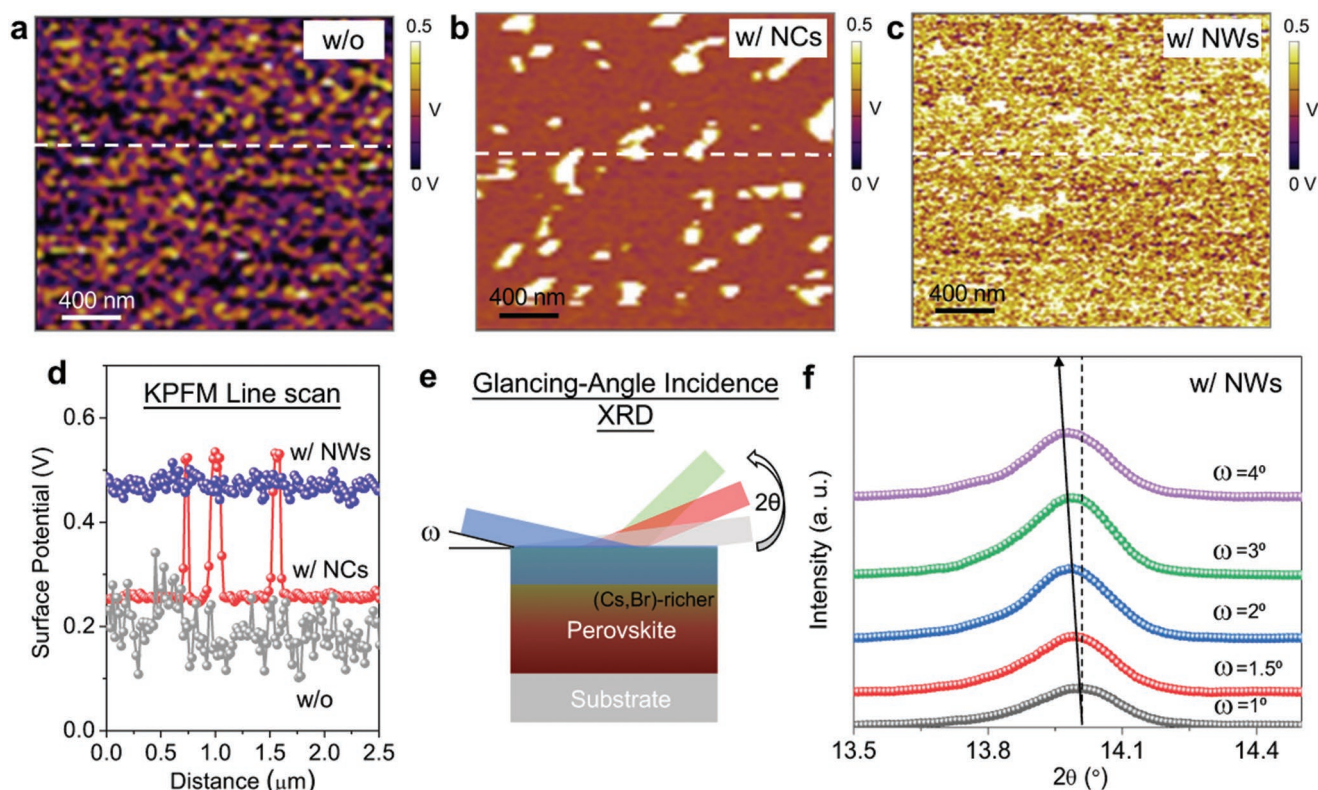


**Figure 4.** KPFM surface potential mapping of the MAPbI<sub>3</sub> perovskite films. a) without nanocrystals, b) with CsPbBr<sub>3</sub>-NCs incorporation, and c) with CsPbBr<sub>3</sub>-NWs incorporation. d) The surface potential variation along the white dashed lines drawn in (a,b,c). e) Illustration of the methodology of glancing-angle XRD. f) Glancing-angle XRD patterns of the MAPbI<sub>3</sub> thin film with CsPbBr<sub>3</sub>-NWs incorporation measured at different glancing angles.

**Figure 3a–c** shows top-view scanning electron microscope (SEM) images of the MAPbI<sub>3</sub> perovskite thin films without nanocrystal, with CsPbBr<sub>3</sub>-NCs incorporation, and CsPbBr<sub>3</sub>-NWs incorporation, respectively. The nanocrystal-free MAPbI<sub>3</sub> perovskite thin film shows typical compact, polycrystalline grain morphology with a mean grain size of 620 nm. In the NCs- and NWs-incorporated cases, the overall morphology is about the same, but the mean grain size is slightly reduced to 555 and 460 nm, respectively. The grain size statistics obtained using image analysis are reported in Figure S3 in the Supporting Information. Correspondingly, the surface roughness (15.3 nm for the nanocrystal-free case) of the MAPbI<sub>3</sub> perovskite thin film is also reduced to 10.2 nm for the NCs case and 7.5 nm for the NWs case, as measured using atomic force microscopy (AFM) (Figure S4, Supporting Information). These morphology changes induced by nanocrystals incorporation can be attributed to the fact that the nanocrystals serve as additional heterogeneous nucleation sites that can boost the nucleation rate during the MAPbI<sub>3</sub> perovskite crystallization process.<sup>[7]</sup> Furthermore, in the NWs-incorporated case, their higher dispersion in solvent is likely to enhance this effect on the film crystallization. Figure 3d shows XRD patterns of MAPbI<sub>3</sub> perovskite thin films without nanocrystals, with CsPbBr<sub>3</sub>-NCs incorporation, and with CsPbBr<sub>3</sub>-NWs incorporation. All the XRD patterns show the characteristic reflections of the MAPbI<sub>3</sub> perovskite (indexed), indicating that no secondary crystalline phases are introduced as a result of the NCs

or NWs incorporation process. The 110 XRD peak in Figure 3e shows no obvious shift, consistent with the low concentration of CsPbBr<sub>3</sub> in the entire bulk of the MAPbI<sub>3</sub> perovskite thin film. The lack of separate XRD peaks and the absence of nanocrystals in top-view SEM suggest that the introduced CsPbBr<sub>3</sub> has been alloyed into the bulk perovskite layer without phase segregation. The time-resolved PL spectra in Figure 3f show much slower PL decay rates after NCs or NWs incorporation. The average PL lifetimes ( $\tau_{\text{Avg}}$ ) for the nanocrystal-free, NCs-incorporated, and NWs-incorporated cases are 37, 126, and 589 ns, respectively. The PL fitting results are shown in Table S1 in the Supporting Information. As discussed above, the grain-boundary density is slightly increased after the nanocrystals incorporation. Thus, the enhanced PL property is attributed to the beneficial passivation of the film surfaces induced by the nanocrystals incorporation, where the more uniform surface-passivation in the NWs case leads to the longest PL lifetime.

Albeit having the same chemical composition, the spatial uniformity of nanocrystal distribution is influenced significantly by the morphology of nanocrystals. Since the concentration of CsPbBr<sub>3</sub> nanocrystals is in fact lower than the detection limits of typical analytical tools (energy dispersive spectroscopy, etc.), surface potential maps of the MAPbI<sub>3</sub> perovskite thin films under continuous illumination with and without nanocrystals-incorporation were obtained using Kelvin-probe force microscopy (KPFM). The results are presented in **Figure 4a–c**. Without nanocrystals, the surface potential is relatively homogeneous

across the film surface. When incorporated with CsPbBr<sub>3</sub> NCs, some areas of the film surface show higher potentials, reflecting an inhomogeneous passivation of the film. However, when CsPbBr<sub>3</sub> NWs are incorporated, the surface potential shows a uniform increase across the entire film surface. These results strongly support our hypothesis that only CsPbBr<sub>3</sub> NWs enable the uniform incorporation across the entire film surface (Figure 2), which is consistent with the PL lifetime results shown in Figure 3f. The line-profiles of the surface-potential mapping images clearly reveal the surface potential variations for the three films as shown in Figure 4d. To delineate the depth profile of the CsPbBr<sub>3</sub> nanocrystals incorporation, glancing-angle ( $\omega$ ) XRD analysis (Figure 4e) was performed. Figure 4f shows the  $\omega$ -dependent XRD patterns of the CsPbBr<sub>3</sub> NWs-incorporated MAPbI<sub>3</sub> perovskite thin film. It is evident that with an increase in  $\omega$ , the 110 peak position of MAPbI<sub>3</sub> shifts gradually to lower  $2\theta$  angles. This observation suggests that there is a gradual expansion of the crystal lattice from the top surface to the bulk film, consistent with the graded-incorporation of CsPbBr<sub>3</sub> into the MAPbI<sub>3</sub> perovskite thin film.

PSC devices using the three types of MAPbI<sub>3</sub> perovskite thin films (without nanocrystals, and with NCs or NWs incorporation) were fabricated by sandwiching the thin films between an FTO/TiO<sub>2</sub> anode and a Spiro-OMeTAD/Au cathode. The typical device architecture is shown in Figure 5a. A scheme of the relative energy-levels is shown in Figure 5b to illustrate the benefit of the CsPbBr<sub>3</sub> nanocrystals incorporation in MAPbI<sub>3</sub> thin films of PSCs. In the nanocrystal-free case, there is a notable energy-level mismatch between HTM HOMO and MAPbI<sub>3</sub> perovskite VBM levels, which leads to insufficient  $V_{OC}$  in PSC devices. After the CsPbBr<sub>3</sub>-nanocrystals incorporation, the VBM of the MAPbI<sub>3</sub> perovskite surface is increased by 0.09 eV (see Figure S5, Supporting Information). However, such VBM increase is not uniform for the NC-incorporated case, which is related to the nonuniform incorporation as discussed above. This nonuniform surface incorporation will result in mixed-electronic structures of the film surface, and, thus, the  $V_{OC}$  enhancement in the final devices is limited. In addition to the enhanced carrier extraction, the laterally uniform incorporation by NWs also provides improved surface passivation according to time-resolved PL (Figure 3f), which is possibly another source for improved device performance. Figure 5c shows the typical current density–voltage ( $J$ – $V$ ) curves (reverse scan) for the PSCs without nanocrystals incorporation, with NCs or NWs incorporation, respectively. The device with NCs shows  $V_{OC}$  of 1.05 V, which is slightly higher than that of 1.04 V for the nanocrystal-free device. However, when NWs are used, the homogeneous surface incorporation (as discussed above) brings up the VBM and thus the device  $V_{OC}$  to 1.12 V (Figure 5c). Consequently, the overall PCE is boosted to 20.18%, compared to 17.42% for the nanocrystal-free PSC and 17.61% for the NCs-incorporated PSC (see inset Table in Figure 5c). Figure 5d shows the  $V_{OC}$  and PCE statistics for the three cases, confirming the high reproducibility of the device performance results. The  $J$ – $V$  hysteresis for a typical PSC with NWs incorporation is shown in Figure 5e. The PCE measured using forward and reverse scans are 20.09% ( $J_{SC}$ : 22.60 mA cm<sup>-2</sup>;  $V_{OC}$ : 1.124 V; FF: 0.791) and 18.75% ( $J_{SC}$ : 22.59 mA cm<sup>-2</sup>;  $V_{OC}$ : 1.113 V; FF: 0.746), respectively. The

current density measured from the  $J$ – $V$  curves is consistent with the integrated current density (21.3 mA cm<sup>-2</sup>) from the external quantum efficiency (EQE) measurement shown in Figure 5f. Since the device exhibits typical hysteresis, the power output at the maximum power point (inset of Figure 5e) is monitored. The PCE of the device stabilizes at  $\approx$ 19%, comparing favorably with that extracted from the reverse-scan  $J$ – $V$  curve.

In addition to the PCE enhancement, the chemical stability of the MAPbI<sub>3</sub> perovskite is also greatly boosted, which represents another important advantage of the CsPbBr<sub>3</sub>-NWs-incorporated perovskite films. Figure 6a,b shows representative XRD patterns of the MAPbI<sub>3</sub> perovskite thin films (nanocrystal-free and NWs-incorporated) before and after 200 h storage under controlled conditions (70% RH, 25 °C). While the nanocrystal-free MAPbI<sub>3</sub> perovskite thin film shows notable decomposition to PbI<sub>2</sub> after storage, the NWs-incorporated film maintains its good phase purity as well as the compact grain morphology (see Figure S6, Supporting Information). It is most likely that the NW-incorporation not only passivates the surface defects (see Figure 3f) and thus slows the moisture ingress kinetics, but also enhances the ionic and/or covalent bonding by incorporating ions (Cs<sup>+</sup> and Br<sup>-</sup>) with smaller radii in the crystalline structure (see Figure 4f). The long-term device stability is also evaluated by operating the PSCs at maximum-power-points continuously under one-sun illumination (unencapsulated, flowing N<sub>2</sub> atmosphere, 40 °C). While the nanocrystal-free PSC shows a decrease of about 16% in PCE after 200 h, only a 4% PCE loss is observed for the NWs-incorporated PSC, demonstrating the promise of CsPbBr<sub>3</sub>-NWs incorporation in enhancing the device stability of PSCs. In addition, the PCE evolution of both PSCs with and without CsPbBr<sub>3</sub>-NWs incorporation as a function of storage time under the same ambient conditions was also monitored, confirming the enhanced ambient stability in the case of NWs incorporation (Figure S7, Supporting Information).

In order to demonstrate the generality of the NWs-incorporation approach for making high-efficiency PSCs, we have used this approach for modifying the perovskite/HTM heterojunction in MA<sub>0.3</sub>FA<sub>0.7</sub>PbI<sub>3</sub>-composition PSCs. This composition of perovskite is known to harvest sunlight more efficiently in the infrared-red region.<sup>[39]</sup> The as-fabricated PSCs based on this mixed-cation halide perovskite show obvious performance enhancement, as compared to PSCs without CsPbBr<sub>3</sub> NWs incorporation, and also PSCs with CsPbBr<sub>3</sub> NCs incorporation (Figure S8, Supporting Information). The “champion” device (Figure 7a) shows  $J_{SC}$  of 24.1 mA cm<sup>-2</sup>,  $V_{OC}$  of 1.12 V, FF of 0.791, and PCE of 21.4% under reverse scan, and  $J_{SC}$  of 24.1 mA cm<sup>-2</sup>,  $V_{OC}$  of 1.11 V, FF of 0.782, and PCE of 20.9% under forward scan. The PCE output at maximum-power-point ( $V = 0.95$  V) is stabilized at  $\approx$ 21% (Figure 7b), which approaches that for those state-of-the-art PSCs.<sup>[13,15,24]</sup> Thus, the NWs-incorporation approach is shown to complement the popular perovskite “composition engineering” methods.<sup>[3]</sup>

### 3. Conclusions

Graded heterojunction PSCs with high lateral uniformity are reported here for the first time by incorporating CsPbBr<sub>3</sub> NWs during the processing of bulk perovskite thin films. Our study

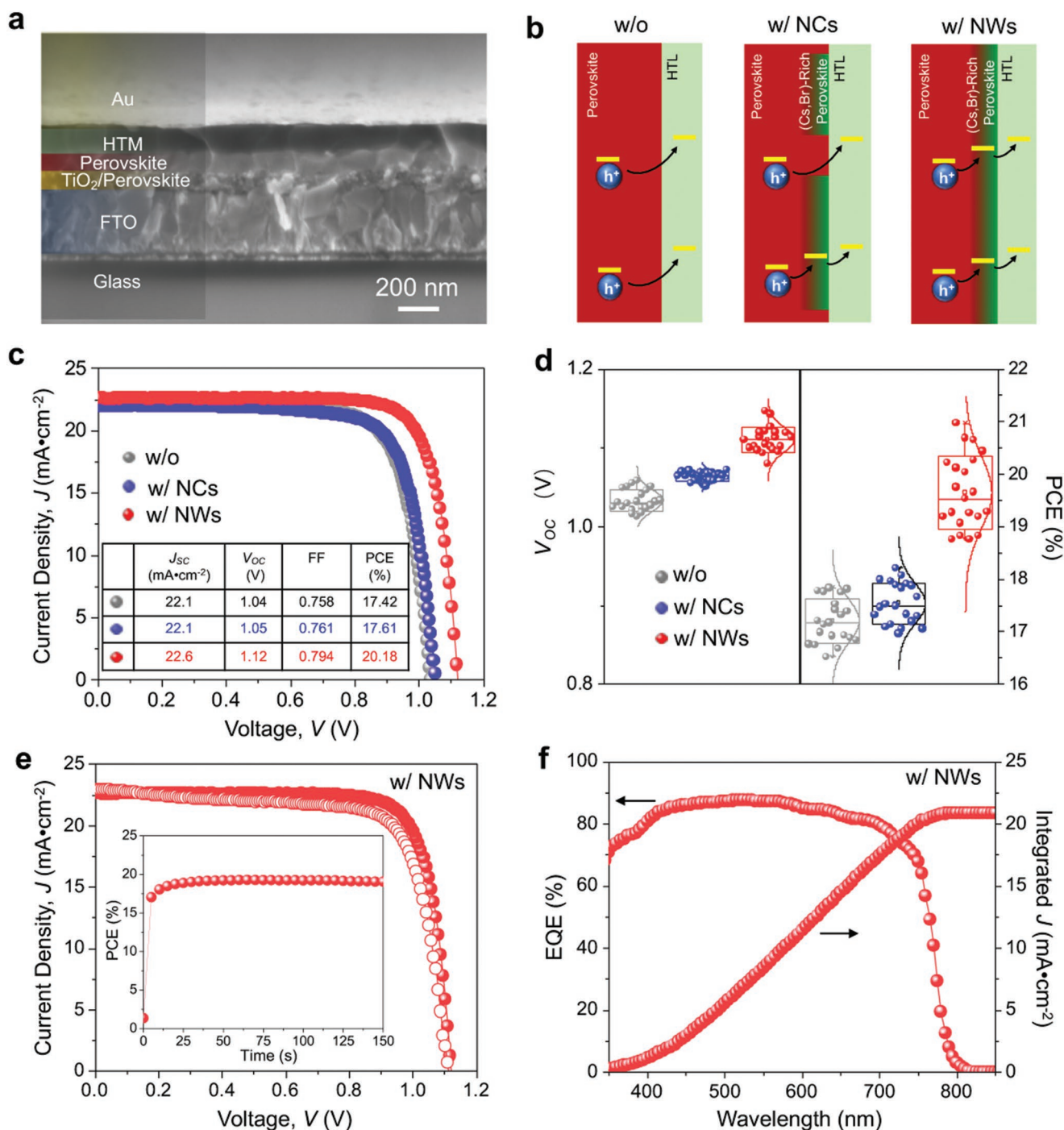


**Figure 5.** a) Cross-sectional SEM image of the PSC using CsPbBr<sub>3</sub> NW-incorporated MAPbI<sub>3</sub> perovskite thin film. b) Schematic representation of the hole-extraction in the PSC without nanocrystals, with CsPbBr<sub>3</sub>-NCs incorporation, and with CsPbBr<sub>3</sub>-NWs incorporation. c)  $J$ - $V$  curves (reverse-scan) and (d) the corresponding PCE statistics of the PSCs without nanocrystal, with CsPbBr<sub>3</sub>-NCs incorporation, and with CsPbBr<sub>3</sub>-NWs incorporation. e)  $J$ - $V$  hysteresis of the PSC with CsPbBr<sub>3</sub>-NWs incorporation. Inset is the maximum-power-point power output of this PSC. f) EQE and integrated current density of the “champion” PSC.

reveals that the nanowire morphology is of vital importance for achieving uniform lateral incorporation of CsPbBr<sub>3</sub> nanocrystals into bulk perovskite thin films that favors the formation of near-ideal perovskite/HTL heterojunction for high-efficiency PSCs. In addition, the surface-incorporation by CsPbBr<sub>3</sub> NWs

can lead to enhanced passivation of the bulk perovskite thin film surfaces, stabilizing the PSCs. The incorporation of nanowires within bulk perovskite thin films surfaces represents a new strategy for making efficient and stable PSCs with engineered interfaces.

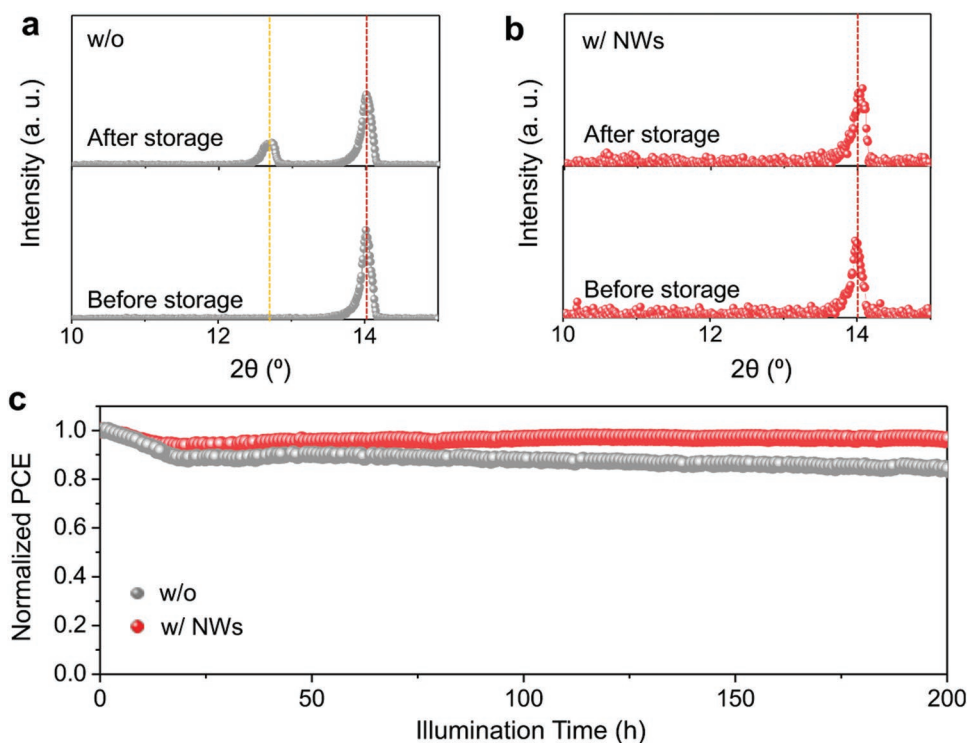


**Figure 6.** Long-term stability of the perovskite thin films and devices. Representative XRD patterns of the MAPbI<sub>3</sub> perovskite thin films before and after 200 h storage under controlled conditions (70 RH%, 25 °C): a) without nanocrystals, b) with CsPbBr<sub>3</sub>-NWs incorporation. The yellow and red dashed lines indicate the peak positions of 001 reflection of the PbI<sub>2</sub> crystal phase and 110 reflection of the MAPbI<sub>3</sub> perovskite phase, respectively. c) Long-term operational stability (under continuous one-sun illumination, unencapsulated, flowing N<sub>2</sub> atmosphere, 40 °C) of PSC devices made without nanocrystals and with CsPbBr<sub>3</sub>-NWs incorporation.

#### 4. Experimental Section

**Synthesis of Perovskite Nanocrystals:** Cesium-oleate was first synthesized by heating 0.625 mmol of Cs<sub>2</sub>CO<sub>3</sub> (Sigma-Aldrich, USA) with 2.0 mmol of oleic acid (technical grade, 90%, Sigma-Aldrich, USA) in 10 mL 1-octadecene (technical grade, 90%, Sigma-Aldrich, USA) at 80 °C under vacuum for 30 min. Subsequently, the reaction mixture was heated to 150 °C until the solids were fully dissolved. The solution was cooled down to room temperature and stored as a stock solution for further use. The CsPbBr<sub>3</sub> perovskite NCs were then synthesized using a method reported in the literature,<sup>[28]</sup> with some

modifications. Briefly, 138 mg of PbBr<sub>2</sub> (Sigma-Aldrich, USA) was dissolved in 10 mL of 1-octadecene with 1 mL of oleic acid and 1 mL of oleylamine (technical grade, 70%, Sigma-Aldrich, USA). The mixture was degassed under vacuum at 100 °C for 1 h before heating up to 170 °C under flowing N<sub>2</sub>, and then 0.8 mL of cesium-oleate solution was rapidly injected into the solution. Within 30 s after injection, the reaction solution was cooled down to room temperature in an ice-water bath. NCs were separated by centrifuge at 8000 rpm for 5 min, and they redispersed in hexane (Fisher Scientific, USA). The resultant NCs were purified by two rounds of precipitation-redispersion process using ethyl acetate (Fisher Scientific, USA) and hexane. The

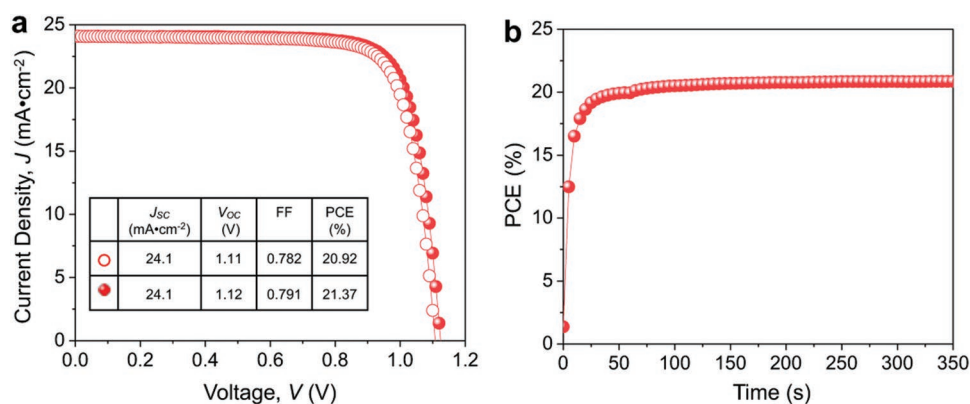


**Figure 7.** a) J–V curves at reverse and forward scans of the "champion" PSC device based on CsPbBr<sub>3</sub>-NWs incorporated MA<sub>0.7</sub>FA<sub>0.3</sub>PbI<sub>3</sub>-composition bulk perovskite thin films. Solid circle: reserve scan; open circle: forward scan. Inset table includes the extracted J–V parameters. b) Stabilized maximum-power-point power output of this PSC.

purified NCs were redispersed in hexane or chlorobenzene (Fisher Scientific, USA) forming a clear solution for further use. CsPbBr<sub>3</sub> NWs were synthesized also using a method reported in the literature,<sup>[29]</sup> with some modifications. In a glass vial, 1.25 mL of hexane was mixed with 0.125 mL of oleic acid and 0.125 mL of oleylamine, to that vial 0.1 mL of cesium-oleate solution was added. Swiftly added to that reaction solution was 0.2 mL of 0.4 M PbBr<sub>2</sub> in DMF (Sigma-Aldrich, USA) under vigorous stirring. At 10 s after injection, 5 mL of acetone was added to the vial. The solution was allowed to react for 5 min before the NWs were separated from the solution using centrifuge at 6000 rpm for 5 min. The resulting NWs were then redispersed in hexane or chlorobenzene for further use.

**Preparation of Perovskite Thin Films:** MAPbI<sub>3</sub> precursor solution (1.3 M) was prepared by dissolving MAI and PbI<sub>2</sub> in 1:1 molar ratio in DMF. Similarly, MA<sub>0.3</sub>FA<sub>0.7</sub>PbI<sub>3</sub> precursor solution (1.3 M) was prepared by dissolving MAI, FAI, and PbI<sub>2</sub> in 0.3:0.7:1 molar ratio in DMF (Sigma-Aldrich, USA). Subsequently, the precursor solutions were spin-coated onto substrates at 1000 rpm for 10 s, followed by 5000 rpm for 30 s. After spinning at 5000 rpm for 10 s, 100  $\mu$ L of chlorobenzene was dripped on to the film. The as-formed solid thin films were annealed at 100 °C for 20 min, resulting in MAPbI<sub>3</sub> or MA<sub>0.3</sub>FA<sub>0.7</sub>PbI<sub>3</sub> perovskite thin films. For depositing MAPbI<sub>3</sub> or MA<sub>0.3</sub>FA<sub>0.7</sub>PbI<sub>3</sub> perovskite thin films with CsPbBr<sub>3</sub> NCs and NWs incorporation, 1 mg ml<sup>-1</sup> CsPbBr<sub>3</sub> NCs or NWs colloidal suspension in chlorobenzene were, respectively, used for the dripping instead of the pure chlorobenzene solvent.

**Nanocrystals Characterization:** UV-vis absorption spectra were measured using a spectrophotometer (Cary 5000, Agilent Technologies, USA). PL spectra of CsPbBr<sub>3</sub> NCs and NWs were measured on a fluorescence spectrometer using 365 nm excitation (FS5, Edinburgh Instruments, UK). TEM characterization was performed using a 2100F TEM (JEOL, Japan) operated at 200 kV. For the TEM sample preparation, the NCs or NWs were directly drop-cast onto TEM grids and dried under ambient conditions. Powder XRD patterns were obtained on a diffractometer (D8 Discovery, Bruker, Germany) using Cu K $\alpha$  radiation. The CsPbBr<sub>3</sub> NCs and NWs samples were prepared by drop-casting onto glass slides for XRD characterization.

**Thin Film Characterization:** XRD patterns were acquired using a high-resolution diffractometer (D8 Advance, Bruker, Germany) with Cu K $\alpha$  radiation. The glancing incidence angle XRD measurements were carried out with glancing angle ranging from 1° to 4°. UV-vis spectra were obtained using a spectrophotometer (UV-2600, Shimadzu, Japan). The microstructures were observed using a SEM (LEO 1530VP, Carl Zeiss, Germany). Ultraviolet photoelectron spectroscopy (UPS) spectra were recorded on a UPS system (5600, PHI, USA). The steady-state and time-resolved PL spectra were recorded using a lab-built spectrophotometer under 395 nm excitation. The PL lifetime was obtained by fitting the time-resolved PL spectra using biexponential decay functions. The AFM measurements with white LED were performed using a versatile AFM (MFP-3D Origin, Asylum Research, USA) in contact mode using conducting Ti/Ir-coated probe tips (ASYELEC.01-R2, Asylum Research, USA).

**Device Fabrication and Testing:** Patterned FTO glass substrates (Hartford Glass, USA) were cleaned sequentially with detergent solution, acetone, and isopropanol. TiO<sub>2</sub> ETL (20 nm) was deposited by spray pyrolysis at 450 °C. The stock solution used for the spray pyrolysis was prepared by mixing 0.2 mL of titanium diisopropoxide bis(acetylacetonate) (TAA) solution (Sigma-Aldrich, USA) with 6 mL of anhydrous ethanol. A 200 nm mesoporous TiO<sub>2</sub> layer was deposited by spin-coating (2000 rpm for 10 s) using a commercial TiO<sub>2</sub> paste (Dyesol-30NRD, Dyesol, Australia) diluted in ethanol (weight ratio of the TiO<sub>2</sub> paste to ethanol was 9:1). The as-coated TiO<sub>2</sub> thin film was dried on a hotplate at 80 °C, and then sintered at 500 °C for 20 min. This was followed by the deposition of the perovskite layer according to the procedure described above. The HTL solution was prepared by dissolving 91 mg of Spiro-OMeTAD (Merck) with additives in 1 mL of chlorobenzene. To this solution, 21  $\mu$ L of Li-bis(trifluoromethanesulfonyl) imide from the stock solution (520 mg in 1 mL of acetonitrile), 16  $\mu$ L of FK209 [tris(2-(1H-pyrazol-1-yl)-4-tert-butylpyridine)-cobalt(III) tris(bis(trifluoromethylsulfonyl)imide) (375 mg in 1 mL of acetonitrile), and

36  $\mu$ L of 4-tertbutylpyridine were added. The HTL was formed by spin-coating the solution at 4000 rpm for 20 s. Finally, 80 nm thick Au electrode was deposited on the top of HTL by thermal evaporation. The *J*-*V* characteristics of the PSCs were measured using a 2400 Sourcemeter (Keithley, USA) under simulated one-sun AM1.5G 100 mW cm<sup>-2</sup> intensity (Oriel Sol3A Class AAA, Newport, USA), under both reverse (from *V*<sub>OC</sub> to *J*<sub>SC</sub>) and forward (from *J*<sub>SC</sub> to *V*<sub>OC</sub>) scans. The step voltage was 5 mV with a 10 ms delay time per step. The maximum-power output stability of PSCs was measured by monitoring the *J* output at the maximum-power-point *V* bias (deduced from the reverse-scan *J*-*V* curves) using the 2400 SourceMeter. A typical active area of 0.12 cm<sup>2</sup> was defined using a nonreflective mask for the *J*-*V* measurements. The stabilized output PCE was calculated using the following relation: PCE = *J* (mA cm<sup>-2</sup>) × *V* (V)) / (100 (mW cm<sup>-2</sup>)). A shutter was used to control the one-sun illumination on the PSC. The EQE spectra were obtained using a quantum-efficiency measurement system (Oriel IQE 200B, Newport, USA). The PSC stability was evaluated by measuring the *J*-*V* characteristics of PSCs after storing the cells in controlled environment for a certain period of time in a climate chamber (HPP110, Memmert, Germany). Unencapsulated PSCs were placed in a sealed holder with a transparent glass cover. A flow of N<sub>2</sub> gas was continuously passed through the holder to minimize the water and oxygen content. *J*-*V* curves were measured every 2 h under one-sun illumination while maintaining the PSCs temperature at  $\approx$ 40 °C. Between the *J*-*V* measurements, the PSCs were biased at maximum-power-point voltages using a potentiostat under continuous one-sun illumination. Additional stability experiments were performed, where unencapsulated PSCs were stored under laboratory ambient conditions, and their PCEs under one-sun illumination were measured about every 25 h.

## Supporting Information

Supporting Information is available from the Wiley Online Library or from the author.

## Acknowledgements

Y.Z. and H.Y. contributed equally to this work. Y.Z., N.P.P., O.C., Y.Z., and M.C. acknowledge the support from the National Science Foundation (OIA-1538893). H.Y. and O.C. acknowledge the support from the Brown University startup funds. Y.Z., O.C., Y.Z., and H.Y. also thank the support from the Brown University's Institute for Molecular and Nanoscale Innovation (IMNI) Seed fund. The authors thank Mr. W. Li for his experimental assistance.

## Conflict of Interest

The authors declare no conflict of interest.

## Keywords

halide perovskites, heterojunction, morphology control, nanocrystals, solar cells

Received: January 21, 2019

Revised: February 18, 2019

Published online:

[1] N.-G. Park, M. Grätzel, T. Miyasaka, K. Zhu, K. Emery, *Nat. Energy* **2016**, *1*, 16152.

[2] H. J. Snaith, *Nat. Mater.* **2018**, *17*, 372.

- [3] J.-P. Correa-Baena, M. Saliba, T. Buonassisi, M. Grätzel, A. Abate, W. Tress, A. Hagfeldt, *Science* **2017**, *358*, 739.
- [4] A. Kojima, K. Teshima, Y. Shirai, T. Miyasaka, *J. Am. Chem. Soc.* **2009**, *131*, 6050.
- [5] NREL Chart of Best Research-Cell Efficiencies, <https://www.nrel.gov/pv/cell-efficiency.html> (accessed: February 2019).
- [6] S. D. Stranks, P. K. Nayak, W. Zhang, T. Stergiopoulos, H. J. Snaith, *Angew. Chem., Int. Ed.* **2015**, *54*, 3240.
- [7] Y. Zhou, O. S. Game, S. Pang, N. P. Padture, *J. Phys. Chem. Lett.* **2015**, *6*, 4827.
- [8] Y. Zong, Y. Zhou, Y. Zhang, Z. Li, L. Zhang, M.-G. Ju, M. Chen, S. Pang, X. C. Zeng, N. P. Padture, *Chem* **2018**, *4*, 1404.
- [9] Y. Zhang, Z. Fei, P. Gao, Y. Lee, F. F. Tirani, R. Scopelliti, Y. Feng, P. J. Dyson, M. K. Nazeeruddin, *Adv. Mater.* **2017**, *29*, 1702157.
- [10] W. A. Dunlap-Shohl, Y. Zhou, N. P. Padture, D. B. Mitzi, *Chem. Rev.* **2018**, *119*, 3193.
- [11] D. Bi, C. Yi, J. Luo, J.-D. Décoppet, F. Zhang, S. M. Zakeeruddin, X. Li, A. Hagfeldt, M. Grätzel, *Nat. Energy* **2016**, *1*, 16142.
- [12] Y. Zhang, Z. Zhou, F. Ji, Z. Li, G. Cui, P. Gao, E. Oveisi, M. K. Nazeeruddin, S. Pang, *Adv. Mater.* **2018**, *30*, 1707143.
- [13] W. S. Yang, B.-W. Park, E. H. Jung, N. J. Jeon, Y. C. Kim, D. U. Lee, S. S. Shin, J. Seo, E. K. Kim, J. H. Noh, S. I. Seok, *Science* **2017**, *356*, 1376.
- [14] M. I. Saidaminov, J. Kim, A. Jain, R. Quintero-Bermudez, H. Tan, G. Long, F. Tan, A. Johnston, Y. Zhao, O. Vozny, E. H. Sargent, *Nat. Energy* **2018**, *3*, 648.
- [15] Y. Hou, X. Du, S. Scheiner, D. P. McMeekin, Z. Wang, N. Li, M. S. Killian, H. Chen, M. Richter, I. Levchuk, N. Schrenker, E. Spiecker, T. Stubhan, N. A. Luechinger, A. Hirsch, P. Schmuki, H.-P. Steinrück, R. H. Fink, M. Halik, H. J. Snaith, C. J. Brabec, *Science* **2017**, *358*, 1192.
- [16] S. Wang, T. Sakurai, W. Wen, Y. Qi, *Adv. Mater. Interfaces* **2018**, *5*, 1800260.
- [17] H. Zhou, Q. Chen, G. Li, S. Luo, T.-b. Song, H.-S. Duan, Z. Hong, J. You, Y. Liu, Y. Yang, *Science* **2014**, *345*, 542.
- [18] Y. Bai, X. Meng, S. Yang, *Adv. Energy Mater.* **2018**, *8*, 1701883.
- [19] Z. Zhou, S. Pang, Z. Liu, H. Xu, G. Cui, *J. Mater. Chem. A* **2015**, *3*, 19205.
- [20] M. Cha, P. Da, J. Wang, W. Wang, Z. Chen, F. Xiu, G. Zheng, Z.-S. Wang, *J. Am. Chem. Soc.* **2016**, *138*, 8581.
- [21] T. Jesper Jacobsson, J.-P. Correa-Baena, M. Pazoki, M. Saliba, K. Schenk, M. Grätzel, A. Hagfeldt, *Energy Environ. Sci.* **2016**, *9*, 1706.
- [22] Y. Zhou, Z. Zhou, M. Chen, Y. Zong, J. Huang, S. Pang, N. P. Padture, *J. Mater. Chem. A* **2016**, *4*, 17623.
- [23] M. Chen, M.-G. Ju, A. D. Carl, Y. Zong, R. L. Grimm, J. Gu, X. C. Zeng, Y. Zhou, N. P. Padture, *Joule* **2018**, *2*, 558.
- [24] D. Luo, W. Yang, Z. Wang, A. Sadhanala, Q. Hu, R. Su, R. Shivanna, G. F. Trindade, J. F. Watts, Z. Xu, T. Liu, K. Chen, F. Ye, P. Wu, L. Zhao, J. Wu, Y. Tu, Y. Zhang, X. Yang, W. Zhang, R. H. Friend, Q. Gong, H. J. Snaith, R. Zhu, *Science* **2018**, *360*, 1442.
- [25] J.-W. Lee, Z. Dai, T.-H. Han, C. Choi, S.-Y. Chang, S.-J. Lee, N. De Marco, H. Zhao, P. Sun, Y. Huang, Y. Yang, *Nat. Commun.* **2018**, *9*, 3021.
- [26] H. Bian, D. Bai, Z. Jin, K. Wang, L. Liang, H. Wang, J. Zhang, Q. Wang, S. Liu, *Joule* **2018**, *2*, 1500.
- [27] M. V. Kovalenko, L. Protesescu, M. I. Bodnarchuk, *Science* **2017**, *358*, 745.
- [28] C. Liu, M. Hu, X. Zhou, J. Wu, L. Zhang, W. Kong, X. Li, X. Zhao, S. Dai, B. Xu, C. Cheng, *NPG Asia Mater.* **2018**, *10*, 552.
- [29] H. Zai, C. Zhu, H. Xie, Y. Zhao, C. Shi, Z. Chen, X. Ke, M. Sui, C. Chen, J. Hu, Q. Zhang, Y. Gao, H. Zhou, Y. Li, Q. Chen, *ACS Energy Lett.* **2018**, *3*, 30.
- [30] S. Sidhik, D. Esparza, A. Martínez-Benítez, T. Lopez-Luke, R. Carriles, I. Mora-Sero, E. Rosa, *J. Phys. Chem. C* **2017**, *121*, 4239.
- [31] H. Yang, Y. Zhang, K. Hills-Kimball, Y. Zhou, O. Chen, *Sustainable Energy Fuels* **2018**, *2*, 2381.
- [32] L. Protesescu, S. Yakunin, M. I. Bodnarchuk, F. Krieg, R. Caputo, C. H. Hendon, R. X. Yang, A. Walsh, M. V. Kovalenko, *Nano Lett.* **2015**, *15*, 3692.
- [33] D. Armar, A. Stern, D. Rotem, D. Porath, L. Etgar, *Nano Lett.* **2017**, *17*, 1007.
- [34] J. Song, J. Li, X. Li, L. Xu, Y. Dong, H. Zeng, *Adv. Mater.* **2015**, *27*, 7162.
- [35] D. Zhang, Y. Yu, Y. Bekenstein, A. B. Wong, A. P. Alivisatos, P. Yang, *J. Am. Chem. Soc.* **2016**, *138*, 13155.
- [36] M. Imran, F. Di Stasio, Z. Dang, C. Canale, A. H. Khan, J. Shamsi, R. Brescia, M. Prato, L. Manna, *Chem. Mater.* **2016**, *28*, 6450.
- [37] D. K. Schroder, *Semiconductor Material and Device Characterization*, 3rd edn, Wiley-Interscience, New York **2006**.
- [38] Y. Chen, L. Li, Z. Liu, N. Zhou, Q. Chen, H. Zhou, *Nano Energy* **2017**, *40*, 540.
- [39] C. Li, Y. Zhou, L. Wang, Y. Chang, Y. Zong, L. Etgar, G. Cui, N. P. Padture, S. Pang, *Angew. Chem., Int. Ed.* **2017**, *56*, 7674.